ETH zürich

ETH Library

Large eddy simulation of transient combustion and soot recession in the ECN Spray A and D flames

Journal Article

Author(s):
Zhang, Min; Ong, Jiun Cai; Pang, Kar Mun; Bai, Xue-Song; Walther, Jens H.

Publication date:
2022-12-01

Permanent link:
https://doi.org/10.3929/ethz-b-000566916

Rights / license:
Creative Commons Attribution 4.0 International

Originally published in:
Fuel 329, https://doi.org/10.1016/j.fuel.2022.125384

This page was generated automatically upon download from the ETH Zurich Research Collection.
For more information, please consult the Terms of use.

Fuel 329 (2022) 125384

Contents lists available at ScienceDirect

Fuel

journal homepage: www.elsevier.com/locate/fuel

Full length article

Large eddy simulation of transient combustion and soot recession in the ECN Spray A and D flames

Min Zhang [a], Jiun Cai Ong [a,*], Kar Mun Pang [b], Xue-Song Bai [c], Jens H. Walther [a,d]

[a] Department of Mechanical Engineering, Technical University of Denmark, 2800 Kgs. Lyngby, Denmark
[b] MAN Energy Solutions, Teglholmsgade 41, 2450 Copenhagen, Denmark
[c] Division of Fluid Mechanics, Lund University, P.O. Box 118, S221 00 Lund, Sweden
[d] Computational Science and Engineering Laboratory, ETH Zürich, CH-8092 Zürich, Switzerland

ARTICLE INFO

Keywords:
Combustion recession
Soot recession
End-of-injection
LES
ECN

ABSTRACT

This paper presents the numerical results of combustion and soot recession in the Engine Combustion Network (ECN) Spray A and D flames using large eddy simulations (LES). The nominal injector nozzle diameters for the ECN Spray A and D are 90 μm and 186 μm. A two-equation soot model is implemented to model the soot formation and oxidation processes. The numerical model is validated by comparing the simulated and measured data in terms of ignition delay time (IDT), lift-off-length (LOL), and temporal evolution of soot mass. The combustion and soot recession processes are analyzed after the end-of-injection (AEOI). The combustion recession processes are first driven by auto-ignition wave propagation followed also by the convective flow in both the Spray A and D flames. A separated high-temperature flame structure is observed in the Spray A flame due to having small favorable mixture regions for the auto-ignition to occur upstream of the quasi-steady lift-off position AEOI. In contrast, a spatially-continuous high-temperature flame structure is formed in the Spray D flame due to having more ignitable mixture regions upstream of the quasi-steady lift-off position and a higher heat release. Soot recession is observed in the Spray D flame but not in the Spray A flame. This is attributed to the mixture upstream of the quasi-steady state soot region becoming favorable to promote soot formation in the Spray D flame, but it becomes fuel-lean AEOI in the Spray A flame.

1. Introduction

Low temperature combustion (LTC) has been developed as the one of the most important strategies for NOx and soot reduction in the last decades. The LTC strategies include exhaust gas recirculation (EGR), homogeneous charge compression ignition (HCCI), as well as late injection with high swirl, are among the strategies used. However, the LTC strategies were shown to increase unburned hydrocarbon (UHC) and CO emissions during the end-of-injection (EOI) process [1,2]. Combustion recession, which refers to the second-stage ignition appearing upstream of a quasi-steady lift-off position after the end-of-injection (AEOI) [3], is able to consume UHC and thus reduce the amount of UHC in diesel engines [4]. However, combustion recession may be accompanied by soot recession, which refers to soot formation process occuring closer to the injector nozzle AEOI than that during steady state injection [5]. This in turn may lead to more soot emissions. Hence, it is practically and fundamentally important to investigate the transient combustion and soot recession processes AEOI.

Various studies have been carried out to investigate the combustion recession [3,4,6,7]. Skeen et al. [8] and Bolla et al. [9] experimentally observed that the lifted flame propagates back to the injector nozzle during the EOI process. Knox et al. [6] systematically investigated the combustion recession using a one-dimensional (1-D) transient gas-jet mixing chemistry model under different ambient densities, temperatures, oxygen (O_2) levels, as well as different injection pressure. They found that higher ambient density, temperature, and O_2 level increase the likelihood of combustion recession, while a higher injection pressure decreases this likelihood. To further predict the likelihood of combustion recession, Knox et al. [4] developed a scaling methodology which can be applied to a wide range of ambient conditions and injector parameters. Although the 1-D model developed by Knox et al. [6,10] is able to predict the likelihood of combustion recession, this model disregards the three-dimensional (3-D) interaction between the mixing and chemical processes in the turbulent spray flame. Jarrahbashi et al. [3] used 3-D computational fluid dynamics (CFD) to investigate the performance of different chemical mechanisms on combustion recession. They found that a chemical mechanism with more accurate modeling of the low temperature chemistry better predicts the combustion recession

* Corresponding author.
E-mail address: jcong@mek.dtu.dk (J.C. Ong).

https://doi.org/10.1016/j.fuel.2022.125384
Received 30 December 2021; Received in revised form 30 May 2022; Accepted 21 July 2022
Available online 11 August 2022
0016-2361/© 2022 The Author(s). Published by Elsevier Ltd. This is an open access article under the CC BY license (http://creativecommons.org/licenses/by/4.0/).

process. Kim et al. [11] and Fang et al. [12] investigated the role of turbulence–chemistry interaction (TCI) in combustion recession of the Engine Combustion Network (ECN) Spray A flame during the EOI process [13]. They pointed out that the TCI models (e.g., representative interactive flamelets and flamelet generated manifold models) affect the prediction of the combustion recession. During the EOI process in the spray flame, one of the most important parameters to affect combustion recession is the ramp-down profile of injection mass flow rate. Koci et al. [14] experimentally investigated the influence of ramp-down profile on combustion recession in a diesel engine. Their findings suggested that the ramp-down profile has a stronger influence on combustion recession than the ambient conditions. Meanwhile, numerical investigations by Knox et al. [10] and Jarrahbashi et al. [3] found that the combustion recession was suppressed by the fast ramp-down profile of injection mass flow rate. In terms of soot recession, only a few studies are available. Knox et al. [6] experimentally observed the soot formation at the near-nozzle region in the Spray A flame AEOI under the ambient temperature of 900 K and O_2 level of 21% when using both fast and slow ramp-down profiles of injection mass flow rate. Furthermore, their observations suggested that the slow ramp-down profile of injection mass flow rate promotes the soot recession due to its richer fuel–air mixtures near the nozzle, as compared to the fast ramp-down profile of injection mass flow rate.

It should be noted that all the aforementioned experimental and numerical studies were only focused on the ECN Spray A flame. To date, all the numerical studies are performed within the URANS framework. Recently, Maes et al. [15] carried out a series of experimental studies on the spray combustion and soot formation in the ECN Spray D flame which used a larger nozzle injector than the ECN Spray A. In their experiment [15], a soot spike was observed AEOI. They speculated that this spike is due to the combustion and soot recession. However, no detailed investigations were carried out. Setting against these backgrounds, the present study aims to investigate the effects of nozzle diameters on the combustion and soot recession processes AEOI in the ECN Spray A and D flames. Considering that large eddy simulation (LES) has a better prediction of air/fuel mixing than URANS [16], LES of the Spray A and D flames under the ambient temperature of 900 K, density of 22.8 kg/m^3, and 15% O_2 are performed to achieve this objective.

The paper is organized as follows: Descriptions of the target spray setup are provided in Section 2. The numerical methods including spray, combustion, and soot models are described in Section 3. Model validation and discussion on combustion and soot recession are presented in Section 4. Concluding remarks are highlighted in the last section.

2. Target spray setup

The validation of the present model performance are based on the experimental data from the ECN Spray A and D cases. Details about the experimental setup and measurement methods can be found from the ECN [13]. For brevity, the main injection parameters of the Spray A and D cases are described here. The *n*-dodecane ($C_{12}H_{26}$) fuel with a temperature of 373 K is injected through an injector nozzle with the injection pressure of 150 μMPa. The nominal diameter of injector nozzles in the Spray A and D cases are 90 μm and 186 μm, respectively. The profiles of mass flow rate for the Spray A and D cases are shown in Fig. 1. According to the recommendation by ECN [13], the profiles are generated by the virtual generator from CMT utility. The total injected fuel mass for the Spray A and D cases are 11.3 mg and 52.6 mg, respectively. The ambient temperature, density, and O_2 level are 900 K, 22.8 kg/m^3, and 15%, respectively.

3. Numerical modeling

In the present study, the simulation are carried out using OpenFOAM-v1712 where the motion of the liquid phase is modeled in a Lagrangian framework, while the gas phase flow and combustion processes are modeled in an Eulerian framework [17].

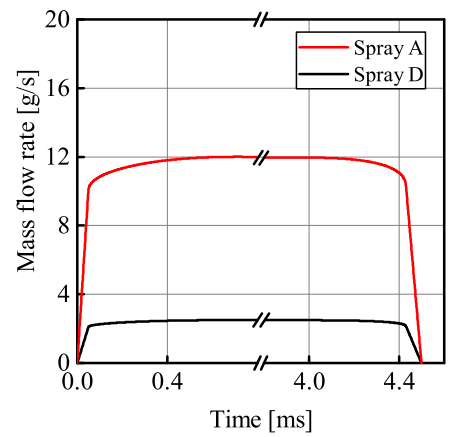

Fig. 1. Profiles of mass flow rate in the Spray A and D cases.

3.1. Gas phase model

The gas phase flow field in the present study is solved by using the Favre-filtered compressible Navier–Stokes equations coupled with a one-equation dynamic structure LES sub-grid-scale model [18,19]. A reduced mechanism developed by Yao et al. [20] is implemented to model the pyrolysis and oxidation of $C_{12}H_{26}$. The partially stirred reactor (PaSR) combustion model is employed to model the turbulence–chemistry-interaction (TCI) [21]. The Taylor time scale is used to account for the mixing time scale between the unburned mixture and burned gases. The mixing constant (C_{mix}) for the Taylor time scale in the PaSR model is set to 0.03, which has been widely used in the spray combustion simulation [21,22].

3.2. Spray model

The discrete liquid phase is modeled using the commonly used Lagrangian particle track method. The injector nozzle is represented as a disc source, from which the Lagrangian parcels are injected within a liquid spray angle of 10°. The size of initial injected parcels is modeled based on a Rosin-Rammler distribution, where the maximum, reference, and minimum droplet size are set to 100%, 70%, and 10% of the nozzle diameter, respectively, which are similarly reported in [23–25]. The Reitz–Diwakar model with a stripping constant of 10 is implemented to model the secondary break-up of droplets. The collision between particles is omitted due to their minor effects on penetration [26]. The evaporation of the discrete phase and heat transfer between liquid and gas phases are modeled based on the Frossling model and Ranz–Marshall method [27,28].

3.3. Soot model

In the present study, the soot formation process is modeled using a two-equation soot model, in which the soot mass fraction (Y_{soot}) and soot particle number density (ϕ_N) are solved [29,30]. The subgrid effects of TCI on the source terms in the two transport equations of the soot model is considered by PaSR model, although no subgrid model is used for turbulence–soot-interaction. Moreover, one-way coupling between the soot and the gas phase is considered.

The transport equations for the two-equation soot model are written as follows,

$$\frac{\partial}{\partial t}(\rho Y_{soot}) + \frac{\partial}{\partial x_j}(\rho u_j Y_{soot}) = \frac{\partial}{\partial x_j}\left(\frac{\mu_t}{Sc_t}\frac{\partial Y_{soot}}{\partial x_j}\right) + \frac{dM_{soot}}{dt} \quad (1)$$

$$\frac{\partial}{\partial t}(\rho \phi_N) + \frac{\partial}{\partial x_j}(\rho u_j \phi_N) = \frac{\partial}{\partial x_j}\left(\frac{\mu_t}{Sc_t}\frac{\partial \phi_N}{\partial x_j}\right) + \frac{1}{N_A}\frac{dN_{soot}}{dt} \quad (2)$$

Table 1
The soot sub-models adopted from [35].

Physical processes	Mathematical expressions
Inception	$\omega_{inc} = 10000\exp\left(\frac{21000}{T}\right)[C_2H_2]$
Surface growth	$\omega_{sg} = 25\left(p/p_{ref}\right)^{\frac{7}{5}}\exp\left(\frac{12100}{T}\right)S_{soot}^{\frac{1}{2}}[C_2H_2]$
Coagulation	$\omega_{cog} = 3\left(\frac{24k_BT}{\rho_{soot}}\right)^{\frac{1}{2}}\left(\frac{6M_{soot}}{\pi\rho_{soot}}\right)^{\frac{1}{6}}N_{soot}^{\frac{11}{6}}$
Oxidation via OH	$\omega_{OH} = 1.146T^{\frac{1}{2}}S_{soot}^{\frac{1}{2}}[OH]$
Oxidation via O_2	$\omega_{O_2} = 10000T^{\frac{1}{2}}\exp\left(\frac{19778}{T}\right)S_{soot}^{\frac{1}{2}}[OH]$

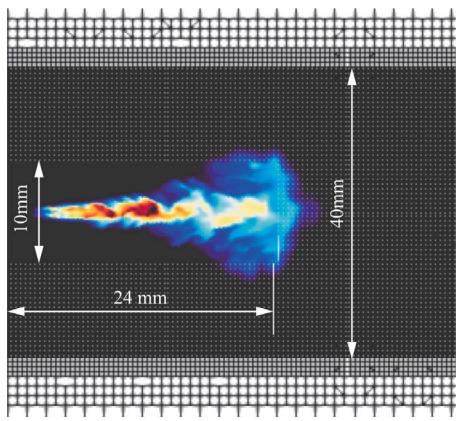

Fig. 2. Cut plane of local mesh configurations.

where ρ and u_j denote the spatially filtered fluid density and flow velocity. μ_t, Sc_t, and N_A denote the turbulent viscosity, turbulent Schmidt number, and Avogadro number, respectively. The turbulent Schmidt number is set to 0.7 [31].

The evolution of soot mass $\left(\frac{dM_{soot}}{dt}\right)$ and soot particle number $\left(\frac{dN_{soot}}{dt}\right)$ is govern by the soot inception, surface growth, coagulation, as well as the oxidation via hydroxyl radicals (OH) and O_2 [28,32]. Acetylene (C_2H_2) is selected as the inception and surface growth species [33,34], while OH and O_2 are selected as oxidizers. The expressions for $\frac{dM_{soot}}{dt}$ and $\frac{dN_{soot}}{dt}$ are given as follows,

$$\frac{dM_{soot}}{dt} = MW_c\left(100\omega_{inc} + 2\omega_{sg} - \omega_{OH} - \omega_{O_2}\right) \tag{3}$$

$$\frac{dN_{soot}}{dt} = N_A\omega_{inc} - \omega_{coag} \tag{4}$$

where MW_c is the molecular weight of carbon atom. The sub-model reaction rates of inception, surface growth as well as oxidation via OH and O_2 are represented by the first to fourth terms on the right hand of Eq. (3). Meanwhile, ω_{coag} denotes the coagulation rate of soot particles.

The formulations of all soot sub-model reaction rates are listed in Table 1. Therein, P, P_{ref}, T, and S_{soot} denote the gas pressure, reference pressure, gas temperature, and soot specific surface area, respectively. The sub-model constants are adopted from [28], except for the surface growth constant which has been tuned to 25 such that the simulated soot mass better corresponds to the measured data [13]. The soot density (ρ_{soot}) and Boltzmann's constant (k_B) are 2000 kg/m^3 and 1.38054×10^{-23} J/K, respectively.

3.4. Numerical schemes and mesh details

The second order schemes are implemented for both temporal and spatial discretization. The time step is set to 50 ns. The computational domain corresponds to the experimental setup which is a cubic chamber with a length of 108 mm for each side [13]. Fig. 2 shows the local mesh configurations to describe the refined region. The mesh size of 0.25 mm is used as the base mesh resolution to cover the spray region. A refined mesh size of 0.125 mm (24 mm axially and 5 mm radially from the location of the injector nozzle) is implemented to cover the liquid region to better resolve the high velocity gradients in that region. In addition to this, a coarser mesh is employed outside of the spray region. The mesh convergence study for the Spray A case can be found in our previous work [35]. The local ratio of the resolved turbulent kinetic energy to the total turbulent kinetic energy is shown in Appendix A. The ratios of resolved turbulence kinetic energy to the total turbulence kinetic energy in the spray region for the Spray A and D cases are 84% and 90%, respectively, thus indicating a sufficient resolution of the flow in the present study [36].

Table 2
Comparison of simulated and experimental IDTs and LOLs.

	Spray A (Sim./Exp.)	Spray D (Sim./Exp.)
IDT (ms)	0.37/0.40	0.44/0.47
LOL (mm)	19.1/16.1	26.7/26.5

4. Results and discussion

4.1. Inert reacting spray characteristics

In the present study, chemically inert spray simulation is first carried out to ensure an accurate prediction of the evaporating spray characteristics in terms of liquid penetration length (LPL) and vapor penetration length (VPL). The LPL is computationally determined by the maximum axial distance from the tip of the injector nozzle to the downstream location where the liquid fuel fraction reaches 95% of its total value [13,37]. It is worth noting that the experimental LPL definition is based on projected liquid volume (PLV). A comparison of the PLV-based, 95% of the liquid mass-based, and experimental LPL for the Spray A case is shown in Appendix B, where they are comparable to one another. The VPL is defined as the farthest axial distance from the injector nozzle tip to the downstream location where a vapor fuel mass fraction of 0.1% is present [13,37]. Fig. 3(a) shows the temporal evolution of LPL and VPL for the Spray A and D cases under inert conditions (0% O_2). As seen in the figure, both LPLs and VPLs show good agreements with the corresponding experimental data for both the Spray A and D cases [13]. Considering that the present study focuses on the recession AEOI, the simulated LPLs are also shown in Fig. 3(b).

4.2. Reacting spray characteristics

After validating the inert spray characteristics, the reacting spray simulation is performed by validating the computed ignition delay time (IDT) and lift-off length (LOL) against the experimental data [13,15]. In the present study, the IDT, as recommend by ECN [13], is defined as the time when the maximum temporal derivative of maximum temperature is observed. The LOL, as used in [38], is defined as the shortest axial distance from the injector nozzle tip to downstream location with the OH mass fraction of 4×10^{-4}. A comparison of the simulated and experimental IDTs and LOLs are listed in Table 2. Both the simulated IDTs and LOLs agree well with the measured data for the Spray A and D flames, respectively. With both the inert and reacting spray characteristics validated, the combustion recession phenomena are studied next.

4.3. Combustion recession

The combustion recession phenomenon refers to the high-temperature combustion appearing upstream of the quasi-steady lift-

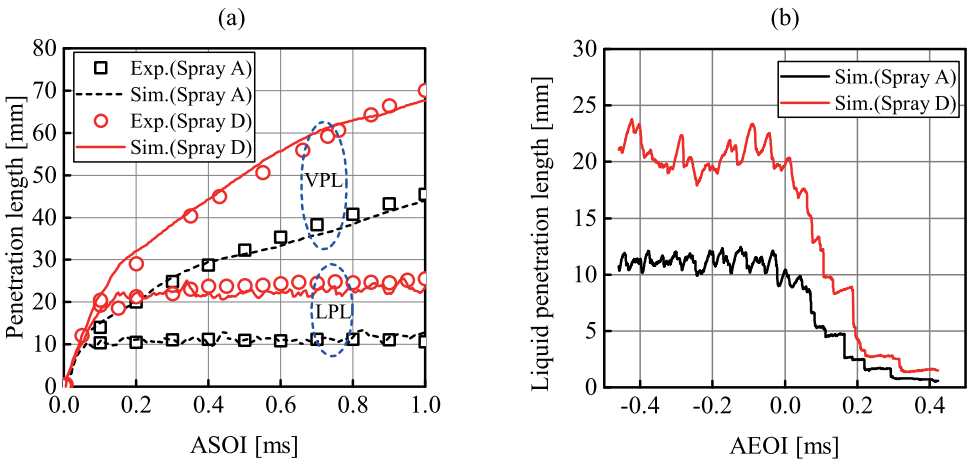

Fig. 3. (a) Temporal evolution of liquid and vapor penetration length (LPL and VPL) for the Spray A and D cases under inert conditions (0%O_2) after start of injection (ASOI). (b) Temporal evolution of simulated LPLs after the end-of-injection (AEOI) in the Spray A and D cases.

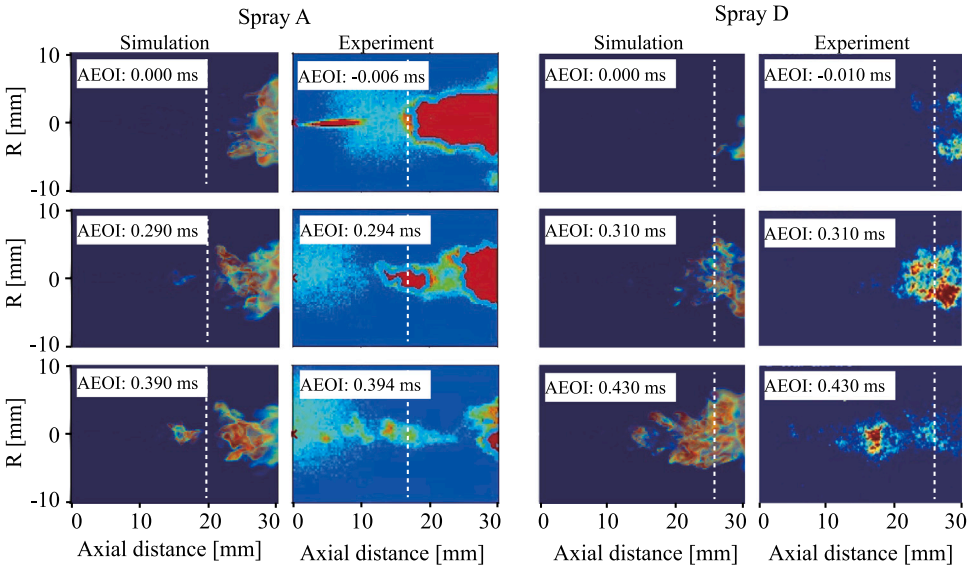

Fig. 4. Comparison of the measured chemiluminescence OH* and the simulated OH distribution after the end-of-injection (AEOI) in the Spray A and D flames [13]. The dashed lines denote the position of quasi-steady lift-off positions before EOI.

off position AEOI [3]. OH is one of the most representative products of high-temperature combustion. Fig. 4 shows a comparison of the measured chemiluminescence OH* and the simulated OH distribution at different time instances AEOI in the Spray A and D flames [13]. From Fig. 4, the measured chemiluminescence OH* and the simulated OH for both the Spray A and D flames appear upstream of the quasi-steady lift-off positions at around 0.30 ms AEOI. This demonstrates that the present LES-PaSR model coupled with Yao mechanism is able to capture the combustion recession. Even without considering TCI effects, it is found that LES-WSR model coupled with Yao mechanism can still capture the combustion recession phenomenon (not shown here). This is, however, opposite to the prediction by Jarrahbashi et al. [3] who failed to predict the combustion recession in their URANS-WSR model coupled with Yao mechanism. One possible reason for the unsuccessful prediction of the combustion recession when using the URANS-WSR framework may be due to the higher scalar dissipation rate predicted (not shown in the present study).

OH is the product of high-temperature combustion as aforementioned, while formaldehyde (CH_2O) is considered here to represent UHC (similarly done in other studies [39,40]). Fig. 5 compares the spatial distribution of OH and CH_2O in the Spray A and D flames at different time instances AEOI. It is apparent that a stronger combustion recession consumes more UHC. This can be observed by comparing the CH_2O distributions in the Spray A and D flames at 0.55 ms AEOI (cf. Fig. 5). A closer examination of the OH distributions shows that the high-temperature region exhibits a separated flame structure in the Spray A flame, while it exhibits a spatially-continuous flame structure in the Spray D flame. This phenomenon is similarly observed in the experiment [10,13] (cf. Fig. 4).

To further investigate the formation of these separated and spatially-continuous high-temperature flame structures during the combustion recession processes in the Spray A and D flames, the temporal evolutions of OH mass/length along the axial direction are shown in Fig. 6. In the Spray A flame, auto-ignition sites occur and grow upstream of the quasi-steady lift-off position from 0.25 ms AEOI onward. One can see that the ignition sites spread towards both upstream and downstream direction and, thus forming a bump (indicated by the arrow in Fig. 6(a)). The axial position of the peak value of this bump seemingly remains constant. Meanwhile, the flame downstream of the quasi-steady lift-off position propagates further away from the injector from 0.30 ms AEOI onward. These collectively lead to the separated high-temperature flame structure observed in the Spray A case. In the Spray

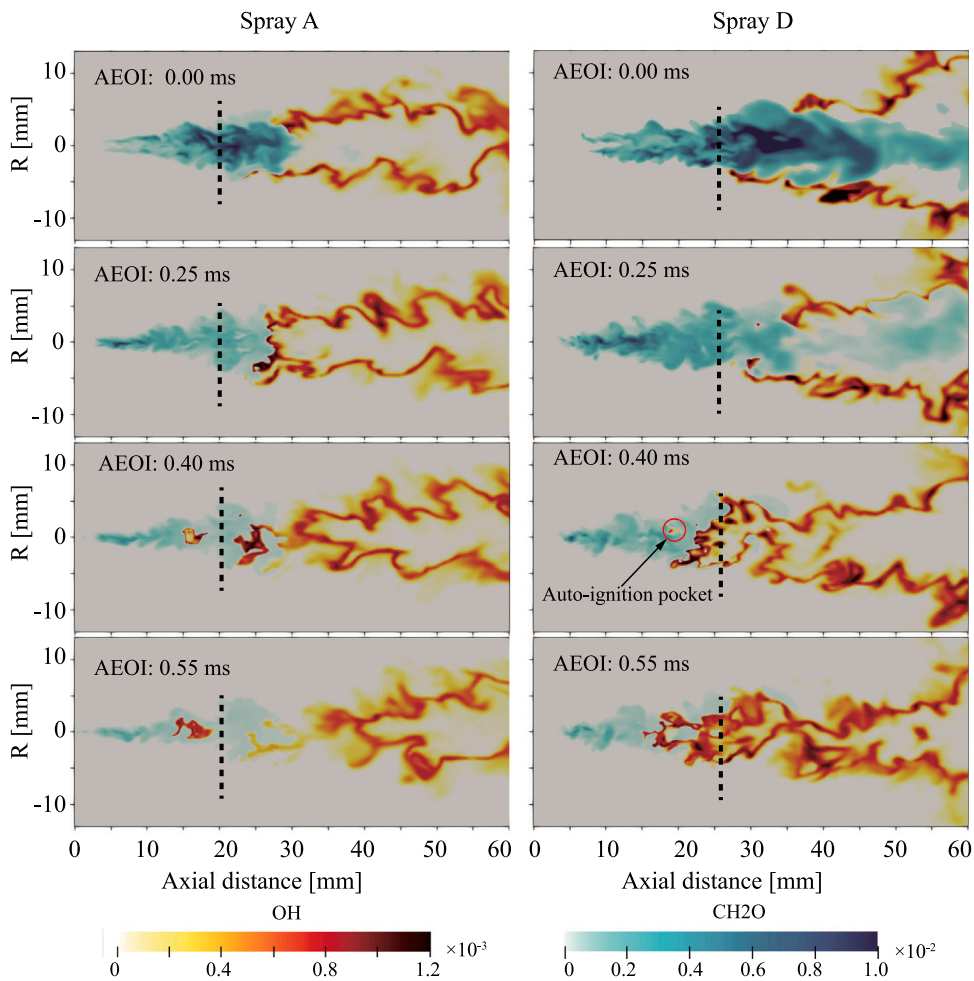

Fig. 5. The temporal evolution of OH–CH_2O after end-of-injection in the Spray A and D flames. The OH and CH_2O are represented by red and blue colors, respectively. The dashed lines denote the position of quasi-steady lift-off positions before EOI. (For interpretation of the references to color in this figure legend, the reader is referred to the web version of this article.)

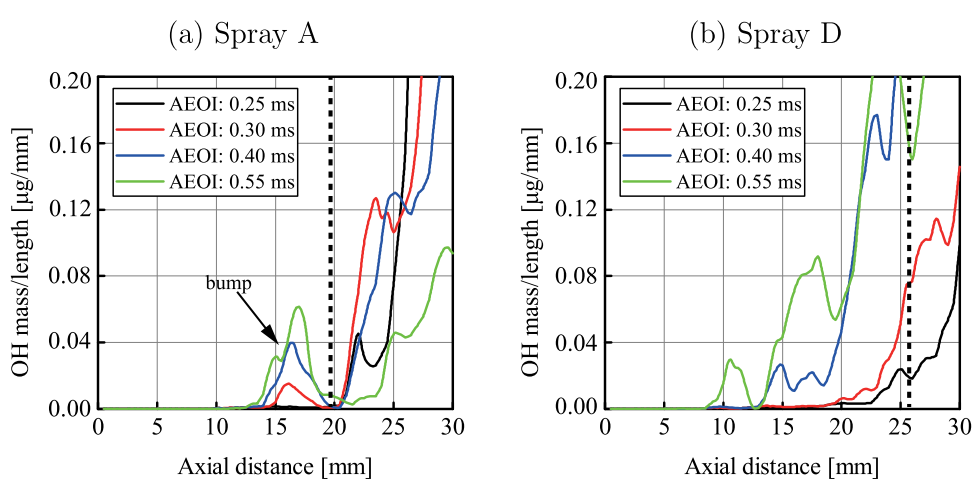

Fig. 6. Temporal evolutions of OH mass/length along the axial direction after end-of-injection in the Spray A and D flames. The dashed lines denote the position of quasi-steady LOLs before EOI.

D flame, the auto-ignition sites at the axial distance of 14 mm starts to occur at 0.35 ms AEOI. Unlike the Spray A flame, the auto-ignition sites in the Spray D flame grow and propagate only towards downstream direction, which is evidently seen by the movement of the position of the peak value. Furthermore, the high-temperature reaction regions near the quasi-steady lift-off position obviously expand towards the upstream location from 0.25 ms AEOI onward. These collectively make the high-temperature reaction regions before and after the quasi-steady lift-off position to merge and, thus resulting in the spatially-continuous high-temperature flame structure in the Spray D case.

Knox et al. [10] suggested that the combustion recession in the Spray A flame is driven by auto-ignition sites occurring independently.

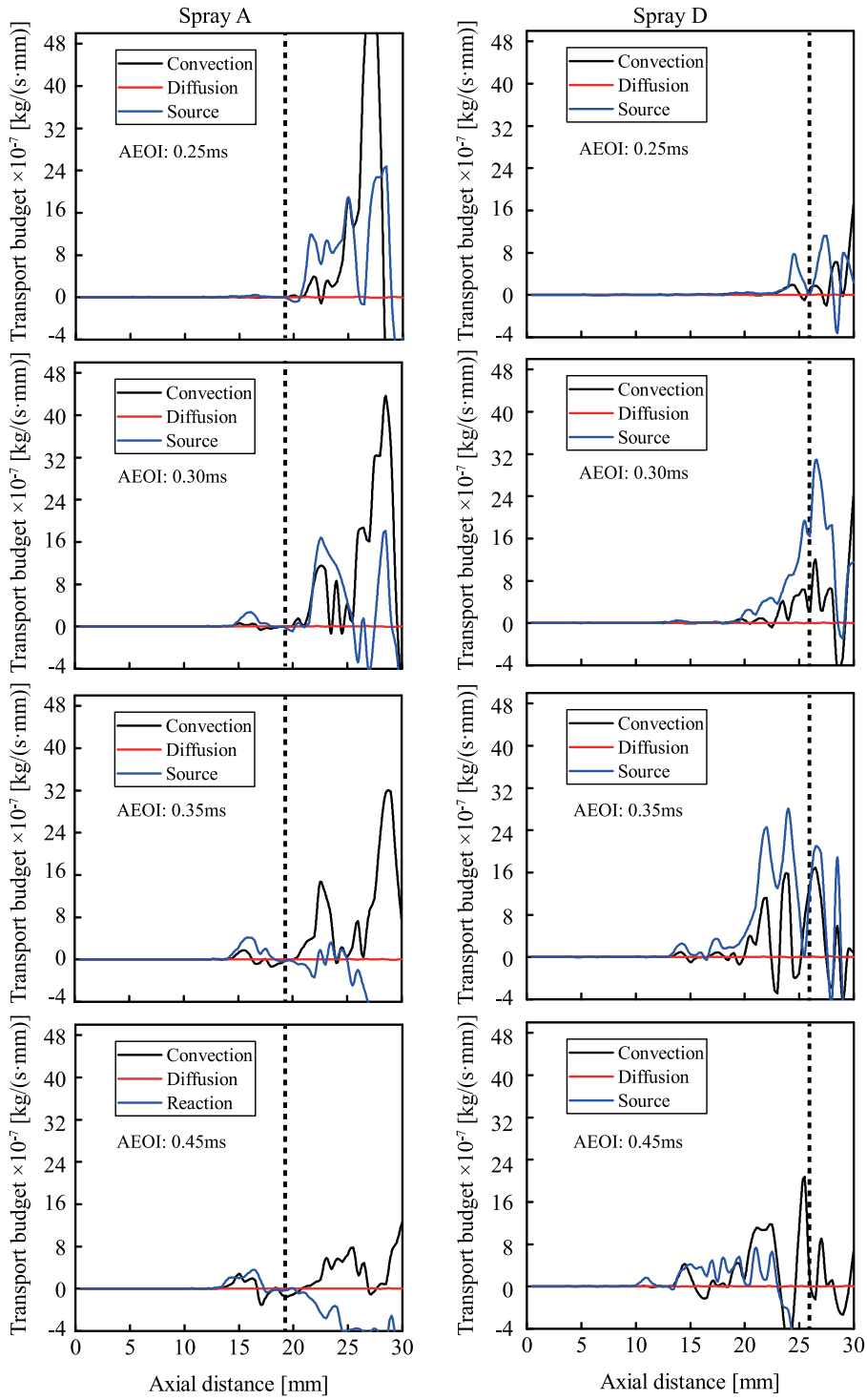

Fig. 7. Comparison of the convection, diffusion, and reaction terms of OH/length along the axial direction after the end-of-injection (AEOI) in the Spray A and D flames. Dashed lines represent the positions of the quasi-steady LOLs before EOI.

However, it is uncertain whether the same underlying mechanism is present in the Spray D flame. In order to further analyze the combustion recession in the Spray A and D flames, a quantitative comparison of transport budgets of OH for the Spray A and D flames is carried out by calculating the convection ($\frac{\partial}{\partial x_i}(\rho u_j Y_{OH})$, where Y_{OH} is mass fraction of OH), diffusion ($D\frac{\partial^2}{\partial x_j{}^2}(\rho Y_{OH})$, where D is effective diffusion coefficient which is the combination of laminar and turbulent diffusion coefficients), and reaction terms ($\dot{\omega}_{OH}$) in the OH transport equation [41]. The comparison of these terms can be found in Fig. 7. It is apparent from Fig. 7 that the diffusion rates of OH in both the Spray A and D flames can be disregarded due to being much lower in magnitude as compared to the other rates. The reaction rates apparently are higher than the magnitudes of the convection rates before 0.35 ms AEOI in both the Spray A and D flames. These collectively indicate that the combustion recession is mainly driven by auto-ignition wave propagation before 0.35 ms AEOI in both the Spray A and D flames. It should be noted that the magnitudes of the convection rates are closer to the reaction rates as time progresses, suggesting that the convection process gradually becomes one of the important drivers for the combustion

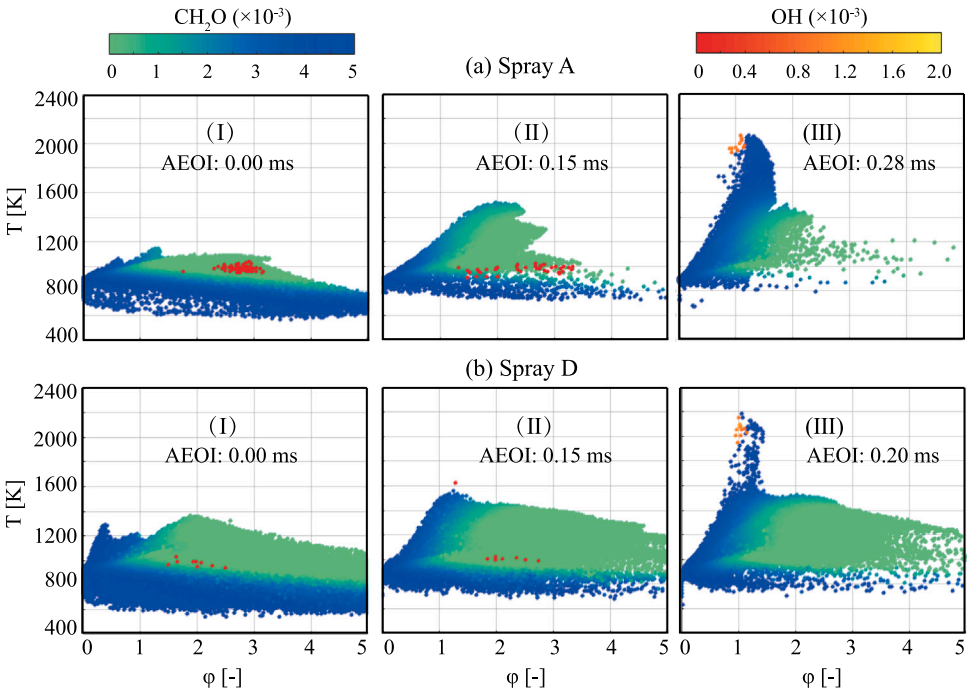

Fig. 8. Scatter plots of equivalence ratio-temperature ($\varphi - T$) at different time instance after the end-of-injection (AEOI) for the Spray A (a(I)–a(III)) and Spray D (b(I)–b(III)) cases. Only CFD cells in the upstream region of the quasi-steady lift-off position are plotted and colored by CH_2O. OH with a threshold of 70% of the maximum mass fraction at their respective time instances is marked as red–yellow color. (For interpretation of the references to color in this figure legend, the reader is referred to the web version of this article.)

recession process. This is more apparent in the Spray D flames, thus suggesting it to be a possible reason for the spatially-continuous high-temperature flame structure to form in the Spray D case as discussed earlier.

As aforementioned, the combustion recession is first governed by the auto-ignition process followed by the convective process as time progresses. It is worth noting that the auto-ignition process is highly dependent on the local equivalence ratio (φ) and the flame temperature. Hence, the scatter plots of equivalence ratio–temperature (φ–T) at different time instances AEOI in the Spray A and D cases are shown in Fig. 8a(I–III) and Fig. 8b(I–III), respectively. It should be noted that only the CFD cells in the upstream region of the quasi-steady lift-off position are considered in the figure. From the figure, it is apparent that the local φ significantly decreases with increasing time in both the Spray A and D flames due to the air entrainment wave [42]. It is worth noting that the local φ is lower and decays faster in the Spray A flame. This can be attributed to the fact that the fuel mass injected during the ramp-down process of the injection in the Spray A case is 5-fold lower than that in the Spray D case. Meanwhile, the large nozzle diameter in the Spray D case gives rise to a larger fuel-rich region and it takes a longer time for the surrounding air to mix into the fuel-rich region. Hence, a significantly larger favorable auto-ignition region is formed upstream of the quasi-steady lift-off position in the Spray D flame than that in the Spray A flame. The larger favorable regions in the Spray D flame support more auto-ignition sites and, thus spatially-continuous high-temperature flame structure is formed.

One can see that the highest flame temperatures at the EOI in both the Spray A and D cases exceed 1000 K. No obvious temperature rise at the fuel-rich side for the Spray A case is observed in Fig. 8a(I), implying that the flame is still at the first stage of ignition. However, the flame temperature appears to increase at the fuel-rich side in the Spray D case, as shown in Fig. 8b(I). This indicates that a transition phase from the first stage of ignition to the second stage of ignition has occurred in the Spray D case at the EOI. For the Spray D case, OH starts to form at the highest flame temperature at 0.15 ms AEOI, indicating the start of high-temperature ignition. At 0.20 ms AEOI, the high-temperature ignition takes place at the stoichiometric conditions. This is similary observed in the Spray A case but at later times. It is worth noting that the observed high-temperature ignition AEOI is different with the observation of high-temperature ignition ASOI in numerous studies [43,44] where the high-temperature ignition takes place at a more fuel-rich side. A closer examination of Fig. 5 shows that the shapes of mixture region in the Spray A and D flames are similar at the EOI. However, the mixture region near the quasi-steady lift-off position becomes wider radially in the Spray D flame as time progresses. This is likely due to the higher fuel mass injected during the ramp-down process of the injection and thus a higher heat release in the Spray D flame, which result in an expansion of the jet [3,45]. To further examine this, the temporal evolution of local heat release rates in the Spray A and D flames are shown in Fig. 9. Although there is no high-temperature ignition upstream of the quasi-steady lift-off position before 0.25 ms AEOI (shown in Fig. 5), the total heat release upstream of the quasi-steady lift-off position in the Spray D flame is still higher than that in the Spray A flame due to the former flame having a larger heat release region.

As mentioned before, there is more than 5-fold fuel mass injected in the Spray D case as compared to the Spray A case. This increases the likelihood of more fuel undergoing first-stage ignition process at the upstream region of the quasi-steady lift-off position, and hence leading to a higher total heat release and a high amount of reactive radicals [6]. This provides a better groundwork for more high-temperature ignitions to occur at this upstream region and, thus resulting in the formation of spatially-continuous flame structure in the Spray D flame AEOI. At 0.35 ms AEOI, both local and total heat release rates are higher in the Spray D flame due to having more high-temperature ignition regions. A higher heat release rate in the Spray D flame implicates a higher flame temperature.

This is further examined in Fig. 10, which shows a comparison of the mean flame temperature as a function of φ at different time instances AEOI in the Spray A and D flames. It should be noted that only the CFD cells upstream of the quasi-steady lift-off position are considered in the figure. It is apparent that the mean flame temperatures at the most of φ

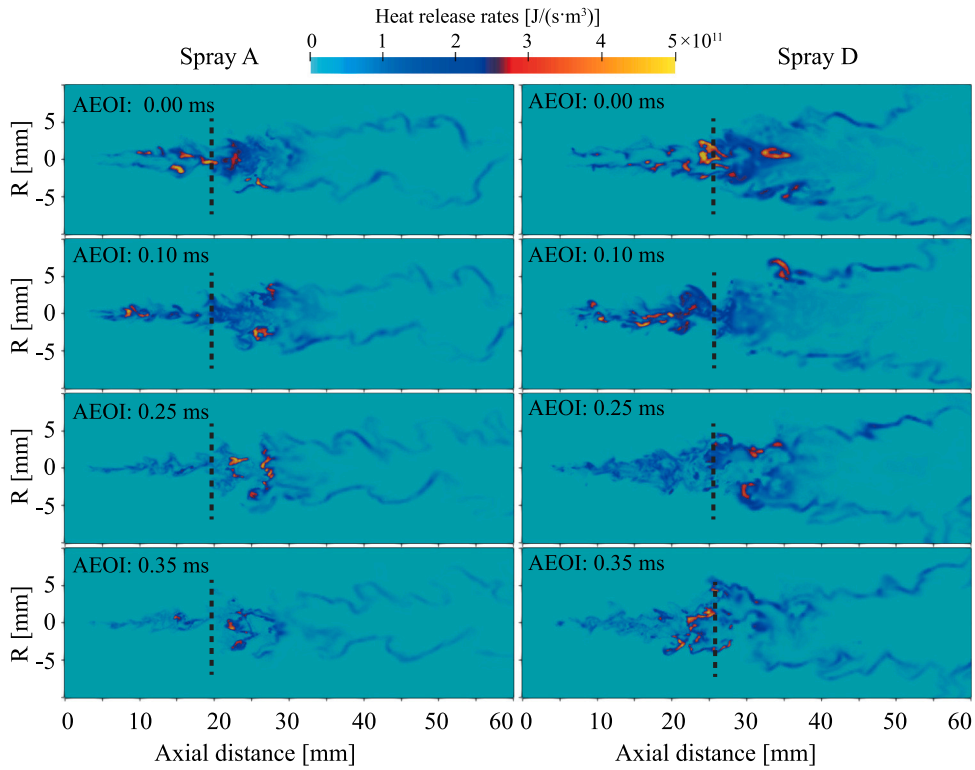

Fig. 9. The temporal evolution of heat release rates after the end-of-injection (AEOI) in the Spray A and D flames. The dashed lines denote the position of quasi-steady LOLs before EOI.

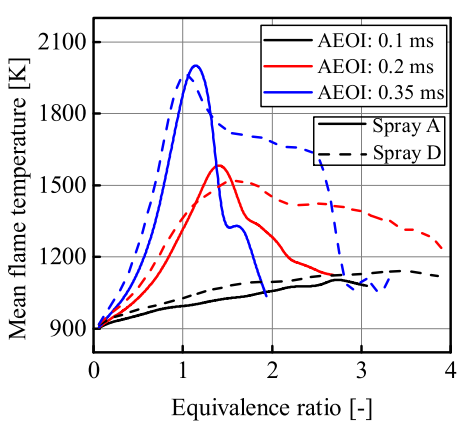

Fig. 10. Comparison of mean flame temperature conditional on equivalence ratio at different time instances after the end-of-injection (AEOI) in the Spray A and D flames. Only the CFD cells upstream of the quasi-steady lift-off position are considered.

are higher in the Spray D flame. Meanwhile, one can see that the local φ in the Spray A flame decays significantly faster than that in the Spray D flame, which corresponds to that depicted in Fig. 8.

4.4. Soot recession

As mentioned in the introduction, the combustion recession may be accompanied by soot recession. Prior to analyzing the soot recession, the soot formation and oxidation processes during the quasi-steady state (QSS) is examined. The examination can be found in authors' previous study [46,47], in which the soot mass and distribution during the QSS were reasonable captured. In the present study, the soot recession refers to the phenomenon where soot forms closer to the injector region AEOI [5]. Fig. 11 shows a comparison of temporal evolution of the simulated and experimental soot mass in the Spray A and D flames. In the experiment, only the soot mass within the regions from the injector nozzle to 67.2 mm and 80 mm in the Spray A and D flames, respectively, are considered. The same regions are implemented in the analysis of the soot mass and scalar calculations of the LES results. It should be noted that the simulation results are ensemble-averaged from 2 realizations, while the experimental results are ensemble-averaged from at least 5 experimental runs. It is worth noting that the soot mass in Spray A case is under predicted. This is likely due to a longer predicted LOL compared to the experimental LOL. One can see that the simulated soot mass shows a good agreement with the measured data in the Spray D flame, whereas the simulated soot mass in the Spray A flame in the final phase shows a delay, as compared to the measured data. The possible reason for this delay is likely due to the uncertainty of the EOI time reported in the experiment. Patel et al. [48] carried out the soot measurement under the Spray A conditions in their new one shot engine (NOSE). The measured soot mass took approximately 0.8 ms AEOI to be fully oxidized, which agrees well with the complete soot oxidation time captured in the present simulated Spray A flame. Furthermore, the simplified chemical mechanism and soot model, C_2H_2 as soot precursor, as well as insufficient LES realizations would contribute to the delay in the final phase of Spray A. Nevertheless, a more obvious soot spike (indicated by an arrow) is captured in the Spray D flame, which are consistent with the experimental observations [13].

Maes et al. [15] speculated that the soot spike observed in the Spray D flame is due to combustion and soot recession. This is further examined in Fig. 12, which shows the distribution of soot volume fraction (SVF) in the Spray A and D flames. One can see that the SVF expands towards downstream region in the Spray A flame, whereas it expands towards the upstream region in the Spray D flame. Moreover, the soot in the central region of the Spray D flame significantly increases from 0 ms to 0.55 ms AEOI, which corresponds the formation of the soot spike in the Spray D flame. These indicate the occurrence of the soot recession in the Spray D flame.

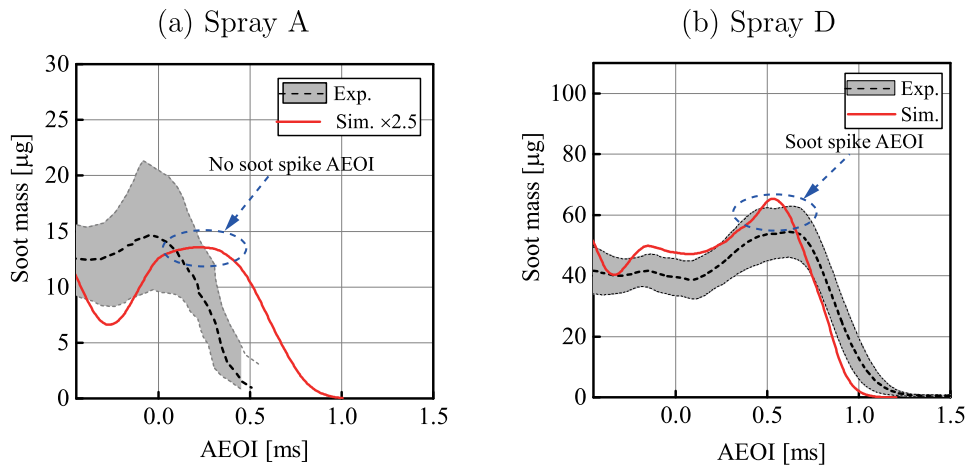

Fig. 11. Temporal evolution of the simulated and experimental soot mass after the end-of-injection (AEOI) in the Spray A and D flames [13]. The simulated soot mass in the Spray A is multiplied by a factor of 2.5.

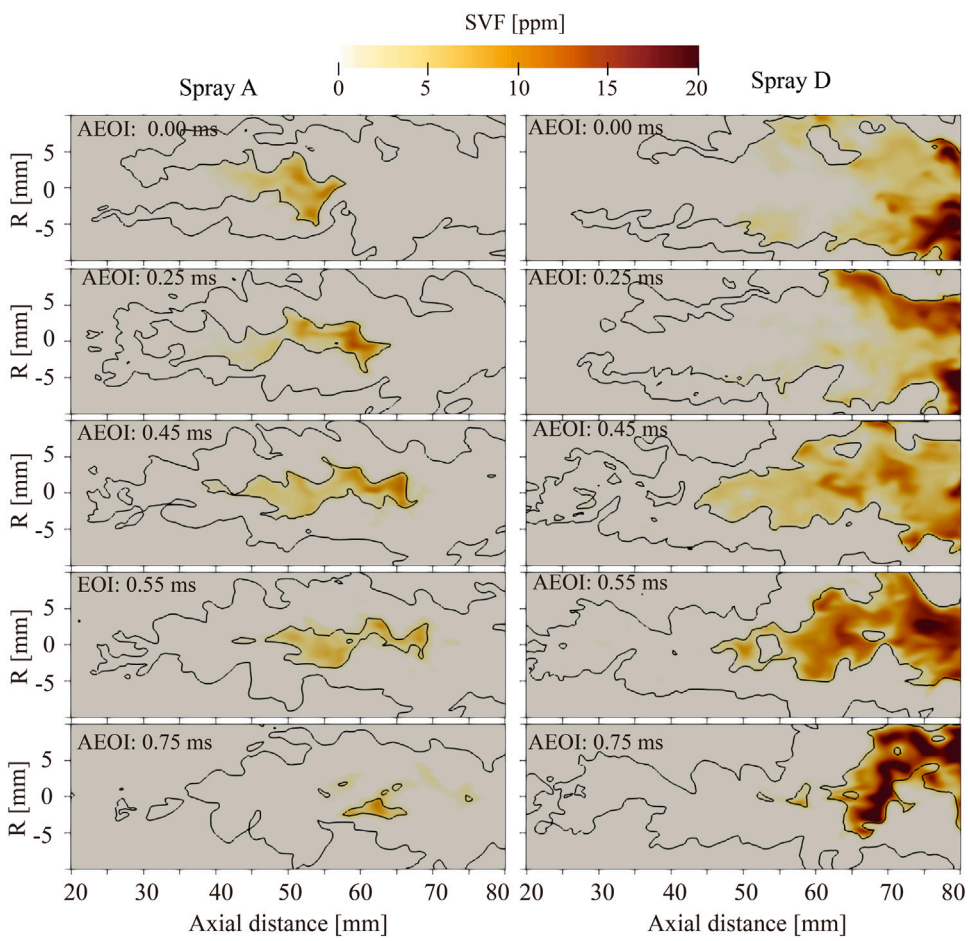

Fig. 12. Temporal evolution of the soot volume fraction (SVF) after the end-of-injection (AEOI) in the Spray A and D flames. The black line represents OH mass fraction of 5×10^{-5}.

To give a clearer visualization of the soot recession, Fig. 13 shows the evolutions of soot mass/length along the axial direction in the Spray A and D flames. The enlarged plots of the red rectangle regions are used to clearly show the evolution of the tail end of the soot region. In the Spray A flame, the tail end of the soot region gradually moves towards downstream AEOI. On the other hand, the tail end of the soot region in the Spray D flame moves towards the injector nozzle from 0 ms to 0.45 ms AEOI but moves towards the downstream region from 0.45 ms AEOI onward. This further indicates that the soot recession occurs in the Spray D flame, but not in the Spray A flame under the present ambient and operating conditions. As mentioned in Section 4.3, the fuel mass injected during the ramp-down process of the injection in the Spray A case is 5-fold lower than that in the Spray D case. Furthermore, a large flame in the Spray D case results in a longer time

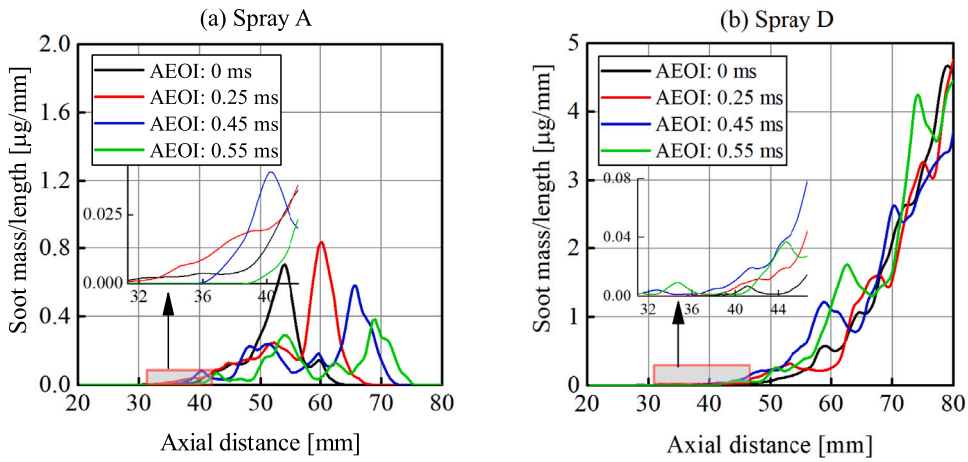

Fig. 13. Temporal evolutions of the soot mass/length along the axial direction after the end-of-injection (AEOI) in the Spray A and D flames.

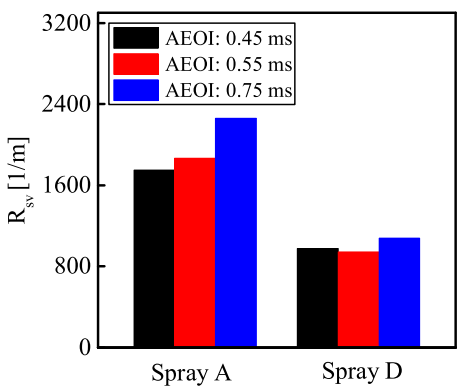

Fig. 14. Ratio of the outer surface area of soot cloud to the soot volume (R_{sv}) after the end-of-injection (AEOI) 0.45 ms in the Spray A and D flames.

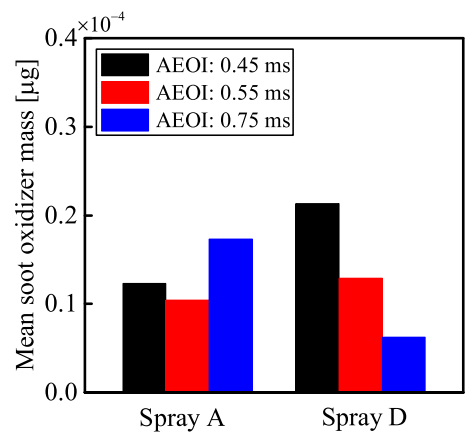

Fig. 15. Comparison of mean soot oxidizer mass after end-of-injection (AEOI) 0.45 ms in the Spray A and D flames.

for the surrounding air to mix into the fuel-rich region. The decay of air entrainment is also faster in the Spray D case. Hence, these collectively lead to the mixture upstream of QSS soot region becoming over fuel-lean before soot onset in the Spray A flame, whereas it becomes a favorable region to promote the soot formation in the Spray D flame.

A closer examination of Fig. 13 reveals that the SVF in the soot-center region becomes higher as time progresses from 0.45 ms AEOI onward in the Spray D flame. In contrast, the SVF in the soot-center region does not change significantly before 0.55 ms AEOI but decreases from 0.55 ms AEOI onward in the Spray A flame. It should be noted that the soot distribution region in the Spray D flame is thicker than that in the Spray A flame. This may result in a weaker soot oxidation and thus higher SVF in the soot-center region in the Spray D flame as time progresses. To examine this, the ratio of outer surface area of soot cloud to the soot volume (R_{sv}) from 0.45 ms AEOI onward in the Spray A and D flames are shown in Fig. 14. The outer surface area of soot cloud is calculated by integrating the surface area of soot iso-surface with 10% of maximum soot mass at its respective time instance. A higher R_{sv} indicates that the soot cloud is easier to be oxidized by OH and O_2 oxidizers due to their stronger oxidative attack on the soot cloud. From Fig. 14, the R_{sv} in the Spray A flame is shown to be higher than that in the Spray D flame. This suggests that the soot in the Spray A flame is easier to be oxidized. From 0.45 ms to 0.75 ms AEOI, the ratio increases in the Spray A flame, but remains relatively unchanged in the Spray D flame as time progresses. The increase of R_{sv} in the Spray A flame results in the decrease of the overall soot region. However, it is expected that the unchanged ratio occurred in the Spray D flame is unable to explain the observation where SVF becomes higher as time progresses. Hence, other possible reasons also play the role in a soot oxidation process from 0.45 ms AEOI onward, especially for the Spray D flame. As shown in Fig. 11, the soot mass starts to decrease around 0.50 ms AEOI, indicating that the soot oxidation dominates over the soot formation process. Therefore, the mean soot oxidizer mass including OH and O_2 from 0.45 ms AEOI onward is compared between the Spray A flame and D flames, as shown in Fig. 15. From 0.45 ms to 0.75 ms AEOI, the mean soot oxidizer mass sightly decreases and then significantly increases in the Spray A flame, whereas it decreases significantly in the Spray D flame as time progresses. In the Spray A flame, the significant increase of the soot oxidizer mass coupled with the increase of R_{sv} at 0.75 ms AEOI results in the stronger soot oxidation and thus lowering the overall SVF of the soot cloud. On the other hand in the Spray D flame, the significant decrease of soot oxidizer mass leads to a weaker soot oxidation in the Spray D flame, leading to a higher SVF in the soot-center region as time progresses.

5. Conclusions

In this study, the combustion and soot regression after the end-of-injection (AEOI) are investigated by performing large eddy simulations of the Engine Combustion Network (ECN) Spray A and D flames at ambient temperature of 900 K, density of 22.8 kg/m^3 and oxygen level of 15%. The nominal injector nozzle diameters for the ECN Spray A and D are 90 μm and 186 μm, respectively.

The combustion recession is observed in both the Spray A and D flames. However, the high-temperature flame structure during the combustion recession process behaves differently. A separated high-temperature flame structure is observed in the Spray A flame, while a spatially-continuous high-temperature flame structure is observed in the Spray D flame. A small favorable mixture region for auto-ignition is present upstream of the quasi-steady lift-off position in the Spray A flame, resulting in the formation of the separated high-temperature flame structure. Conversely, a larger ignitable mixture region is present upstream of the quasi-steady lift-off position in the Spray D flame. This leads to flame downstream of the quasi-steady lift-off position merging with the auto-ignition sites which are upstream of the quasi-steady lift-off position. Meanwhile, a higher total heat release upstream of the quasi-steady lift-off position in the Spray D flame promotes more auto-ignition sites. These collectively contribute to the spatially-continuous high-temperature flame structure in the Spray D flame.

The soot recession appears in the Spray D flame, but not in the Spray A flame. The difference of the soot recession in the Spray A and Spray D flames is attributed to the larger nozzle diameter and higher amount of fuel injected in the Spray D flame. The mixture upstream of the quasi-steady state soot region becomes fuel-lean before soot onset can occur in the Spray A, whereas this mixture becomes a favorable region that promotes soot formation in the Spray D flame. Furthermore, the significant decrease of mean soot oxidizer mass in the soot-center region leads to a weaker soot oxidation in the Spray D flame, which subsequently leads to a higher soot volume fraction as time progresses.

CRediT authorship contribution statement

Min Zhang: Conceptualization, Methodology, Validation, Writing – original draft. **Jiun Cai Ong:** Methodology, Supervision, Writing – review. **Kar Mun Pang:** Conceptualization, Supervision, Writing – review & editing. **Xue-Song Bai:** Supervision, Writing – review. **Jens H. Walther:** Supervision, Writing – review & editing.

Declaration of competing interest

The authors declare that they have no known competing financial interests or personal relationships that could have appeared to influence the work reported in this paper.

Acknowledgments

Min Zhang was sponsored by China Scholarship Council (CSC). Jiun Cai Ong gratefully acknowledged the financial support from the Independent Research Fund Denmark (DFF) and MAN Energy Solutions under the grant number 8022-00143B. The computation was performed using Niflheim cluster at Technical University of Denmark (DTU). The authors acknowledged PRACE for awarding us access to Joliot-Curie at GENCI@CEA, France.

Appendix A. Adiabatic mixing line

Fig. A.1 shows the local ratio of resolved turbulent kinetic energy to the total turbulent kinetic energy in the Spray A and D cases.

Appendix B. Projected liquid volume (PLV)-based LPL

Following the guidance in [49], a comparison of the PLV-based, 95% of the liquid mass-based, and experimental LPL for the Spray A case is shown in Fig. B.1. It is apparent that the LPLs from these two definitions show good agreements with the experimental data.

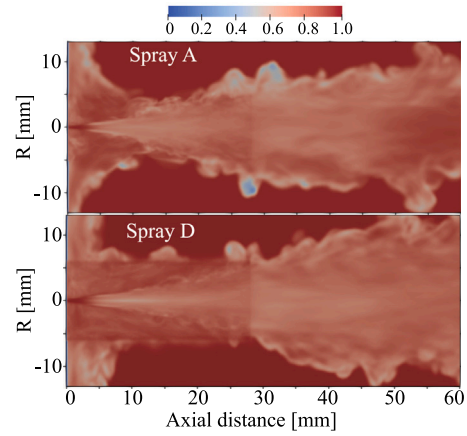

Fig. A.1. Local ratio of resolved turbulent kinetic energy to the total turbulent kinetic energy.

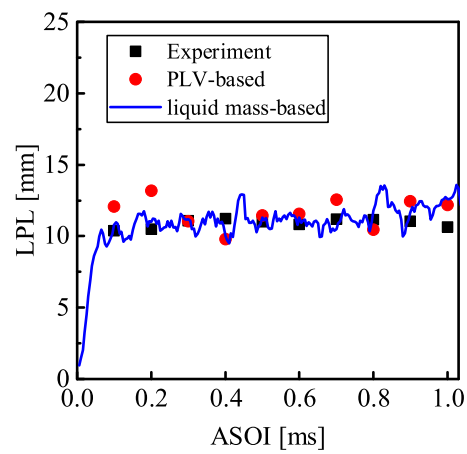

Fig. B.1. Comparison of PLV-based, 95% of the liquid mass-based, and experimental LPLs.

References

[1] Musculus MP, Lachaux T, Pickett LM, Idicheria CA. End-of-injection over-mixing and unburned hydrocarbon emissions in low-temperature-combustion diesel engines. SAE Tech Pap 2007-01-0907 2007.
[2] Lachaux T, Musculus MP. In-cylinder unburned hydrocarbon visualization during low-temperature compression-ignition engine combustion using formaldehyde PLIF. Proc Combust Inst 2007;31:2921–9.
[3] Jarrahbashi D, Kim S, Knox BW, Genzale CL. Computational analysis of end-of-injection transients and combustion recession. Int J Engine Res 2017;18:1088–110.
[4] Knox BW, Genzale CL. Scaling combustion recession after end of injection in diesel sprays. Combust Flame 2017;177:24–36.
[5] Knox BW. End-of-injection effects on diesel spray combustion (PhD Dissertation). Georgia Institute of Technology; 2016.
[6] Knox B, Genzale C. Effects of end-of-injection transients on combustion recession in diesel sprays. SAE Int J Engines 2016;9:932–49.
[7] Fang X, Ismail R, Sekularac N, Davy M. On the prediction of spray a end of injection phenomenon using conditional source-term estimation. SAE Tech Pap 2020-01-0779 2020.
[8] Skeen SA, Manin J, Pickett LM. Simultaneous formaldehyde PLIF and high-speed Schlieren imaging for ignition visualization in high-pressure spray flames. Proc Combust Inst 2015;35:3167–74.
[9] Bobba MK, Genzale CL, Musculus MP. Effect of ignition delay on in-cylinder soot characteristics of a heavy duty diesel engine operating at low temperature conditions. SAE Int J Engines 2009;2:911–24.
[10] Knox BW, Genzale CL, Pickett LM, Garcia-Oliver JM, Vera-Tudela W. Combustion recession after end of injection in diesel sprays. SAE Int J Engines 2015;8:679–95.
[11] Kim S, Jarrahbashi D, Genzale C. The role of turbulent-chemistry interaction in simulating end-of-injection combustion transients in diesel sprays. SAE Tech Pap 2017-01-0838 2017.

[12] Fang X, Ismail R, Davy MH, Camm J. Numerical studies of combustion recession on ECN diesel spray a. In: Internal combustion engine division fall technical conference, Vol. 51999. 2018, p. V002T06A011.
[13] Engine Combustion Network. Available from: https://ecn.sandia.gov/ecn-data-search/.
[14] Koci C, Martin G, Bazyn T, Morrison W, Svensson K, Gehrke C. The influence of diesel end-of-injection rate shape on combustion recession. SAE Int J Engines 2015;8:647–59.
[15] Maes N, Skeen SA, Bardi M, Fitzgerald RP, Malbec L-M, Bruneaux G, et al. Spray penetration, combustion, and soot formation characteristics of the ECN spray C and spray D injectors in multiple combustion facilities. Appl Thermal Eng 2020;172:115136.
[16] Jhavar R, Rutland CJ. Using large eddy simulations to study mixing effects in early injection diesel engine combustion. SAE Tech Pap 2006-01-0871 2006.
[17] Weller HG, Tabor G, Jasak H, Fureby C. A tensorial approach to computational continuum mechanics using object-oriented techniques. Comput Phys 1998;12:620–31.
[18] Liu K, Haworth DC, Yang X, Gopalakrishnan V. Large-eddy simulation of motored flow in a two-valve piston engine: POD analysis and cycle-to-cycle variations. Flow, Turbul Combust 2013;91(2):1–31.
[19] Senecal PK, Pomraning E, Richards KJ, Som S. An investigation of grid convergence for spray simulations using an LES turbulence model. SAE Tech Pap 2013;01–1083.
[20] Yao T, Pei Y, Zhong B-J, Som S, Lu T, Luo KH. A compact skeletal mechanism for n-dodecane with optimized semi-global low-temperature chemistry for diesel engine simulations. Fuel 2017;191:339–49.
[21] Kärrholm FP, Tao F, Nordin N. Three-dimensional simulation of diesel spray ignition and flame lift-off using openFOAM and KIVA-3V CFD codes. SAE Tech Pap 2008-01-0961 2008.
[22] Song B, Seo J, Choi Y. Numerical investigation of a DI diesel spray flame using a detailed chemical reaction mechanism. Int J Automot Technol 2012;13(3):365–72.
[23] D'Errico G, Lucchini T, Contino F, Jangi M, Bai X-S. Comparison of well-mixed and multiple representative interactive flamelet approaches for diesel spray combustion modelling. Combust Theory Model 2014;18(1):65–88.
[24] Desantes JM, García-Oliver JM, Novella R, Pérez-Sánchez EJ. Application of a flamelet-based CFD combustion model to the LES simulation of a diesel-like reacting spray. Comput & Fluids 2020;200.
[25] Ong JC, Pang KM, Bai X-S, Jangi M, Walther JH. Large-eddy simulation of n-dodecane spray flame: Effects of nozzle diameters on autoignition at varying ambient temperatures. Proc Combust Inst 2021;38(2):3427–34.
[26] Jangi M, D'Errico G, Bai X-S, Lucchini T. Numerical simulation of the ECN spray a using multidimensional chemistry coordinate mapping: N-dodecane diesel combustion. SAE Tech Pap 2012-01-1660 2012.
[27] Chishty MA, Bolla M, Hawkes ER, Pei Y, Kook S. Soot formation modelling for n-dodecane sprays using the transported PDF model. Combust Flame 2018;192:101–19.
[28] Pang KM, Jangi M, Bai X-S, Schramm J. Evaluation and optimisation of phenomenological multi-step soot model for spray combustion under diesel engine-like operating conditions. Combust Theory Model 2015;19(3):279–308.
[29] Pang KM, Jangi M, Bai X-S, Walther JH, Schramm J. Modelling of diesel spray flames under engine-like conditions using an accelerated Eulerian stochastic fields method. Combust Flame 2018;183:363–83.
[30] Brookes S, Moss J. Predictions of soot and thermal radiation properties in confined turbulent jet diffusion flames. Combust Flame 1999;116:486–503.
[31] Eberle C, Gerlinger P, Geigle KP, Aigner M. Toward finite-rate chemistry large-eddy simulations of sooting swirl flames. Combust Sci Tech 2018;190:1194–217.
[32] Leung KM, Lindstedt RP, Jones W. A simplified reaction mechanism for soot formation in nonpremixed flames. Combust Flame 1991;87:289–305.
[33] Fernandez SF, Paul C, Sircar A, Imren A, Haworth DC, Roy S, et al. Soot and spectral radiation modeling for high-pressure turbulent spray flames. Combust Flame 2018;190:402–15.
[34] Roy SP, Haworth DC. A systematic comparison of detailed soot models and gas-phase chemical mechanisms in laminar premixed flames. Combust Sci Tech 2016;188(7):1021–53.
[35] Zhang M, Ong JC, Pang KM, Bai X-S, Walther JH. An investigation on early evolution of soot in n-dodecane spray combustion using large eddy simulation. Fuel 2021;293:120072.
[36] Pope SB. Ten questions concerning the large-eddy simulation of turbulent flows. New J Phys 2004;6:1–24.
[37] Pei Y, Hawkes ER, Kook S. A comprehensive study of effects of mixing and chemical kinetic models on predictions of n-heptane jet ignitions with the PDF method. Flow Turbul Combust 2013;91(2):249–80.
[38] Pang KM, Jangi M, Bai X-S, Schramm J, Walther JH. Effects of nozzle diameter on diesel spray flames: A numerical study using an Eulerian stochastic field method. Energy Procedia 2016;142:1028–33.
[39] Cung K, Zhu X, Moiz AA, Lee S-Y, De Ojeda W. Characteristics of formaldehyde (CH2o) formation in dimethyl ether (DME) spray combustion using PLIF imaging. SAE Int J Fuels Lubr 2016;9:138–48.
[40] Olsen DB, Mitchell CE. Formaldehyde formation in large bore engines part 2: Factors affecting measured CH2O. J Engng Gas Turbines Power 2000;122:611–6.
[41] Gordon RL, Masri AR, Pope SB, Goldin GM. Transport budgets in turbulent lifted flames of methane autoigniting in a vitiated co-flow. Combust Flame 2007;151:495–511.
[42] Musculus MP, Kattke K. Entrainment waves in diesel jets. SAE Int J Engines 2009;2:1170–93.
[43] Pei Y, Som S, Pomraning E, Senecal PK, Skeen SA, Manin J, et al. Large eddy simulation of a reacting spray flame with multiple realizations under compression ignition engine conditions. Combust Flame 2015;162:4442–55.
[44] Kahila H, Wehrfritz A, Kaario O, Masouleh MG, Maes N, Somers B, et al. Large-eddy simulation on the influence of injection pressure in reacting spray A. Combust Flame 2018;191:142–59.
[45] Jarrahbashi D, Kim S, Genzale CL. Simulation of combustion recession after end-of-injection at diesel engine conditions. J Engng Gas Turbines Power 2017;139.
[46] Zhang M, Ong JC, Pang KM, Bai X-S, Walther JH. Large eddy simulation of soot formation and oxidation for different ambient temperatures and oxygen levels. Appl Energy 2022;306:118094.
[47] Zhang M, Ong JC, Pang KM, Bai X-S, Walther JH. Effects of ambient CO2 and H2O on soot processes in n-dodecane spray combustion using large eddy simulation. Fuel 2022;312:122700.
[48] Patel C, Hespel C, Nguyen TL, Foucher F, Mounaïm-Rousselle C. Effect of exhaust gas recirculation composition on soot in ECN spray a conditions. Oil Gas Sci Technol–Rev DIFP Energies Nouvelles 2020;75:34.
[49] Nguyen TM, Dahms RN, Pickett LM, Tagliante F. The corrected distortion model for Lagrangian spray simulation of transcritical fuel injection. Int J Multiphase Flow 2022;148:103927.